Journal of Materials Research and Technology 36 (2025) 6578–6589

Contents lists available at ScienceDirect

Journal of Materials Research and Technology

journal homepage: www.elsevier.com/locate/jmrt

Improvement of toughness and wear resistance in PBT composites via synergistic reinforcement of functionalized phenolic microspheres and tungsten carbide

Jaeyeon Kim [a], Jaekyung Lee [a], Oju Kwon [a], Subin Lee [b], Pei-Chen Su [c], Minhaeng Cho [d], Jooheon Kim [a,b,*]

[a] School of Chemical Engineering, Chung-Ang University, Seoul, 06974, Republic of Korea
[b] Department of Intelligent Energy and Industry, Graduate School, Chung-Ang University, Seoul, 06974, Republic of Korea
[c] School of Mechanical and Aerospace Engineering, Nanyang Technological University, Singapore
[d] School of Mechanical Engineering, Chung-Ang University, Seoul, 06974, Republic of Korea

ARTICLE INFO

Handling editor: P Rios

Keywords:
Wear resistance
Phenol-paraformaldehyde resin
Thermal conductivity
Polybutylene terephthalate

ABSTRACT

The demand for high-performance polymer composites has driven research to enhance the mechanical, thermal, and tribological properties of polybutylene terephthalate (PBT). However, neat PBT suffers from limitations such as low thermal conductivity and poor wear resistance. To address these issues, we developed PBT composites reinforced with functionalized phenolic microspheres (FPM-BDO) and 3-mercaptopropyl trimethoxysilane-modified tungsten carbide (M − WC). The resulting FPM-BDO/M-WC/PBT composites exhibited significant improvements. The percolated heat conduction networks formed by M − WC increased thermal conductivity to 0.627 W/m·K, a 129 % enhancement over neat PBT. The addition of FPM-BDO improved crystallization, increasing crystallinity and tensile strength by 20.3 % while maintaining 94.3 % of the original elongation at break, overcoming the brittleness of neat PBT. Tribological performance was also enhanced, with a 46.1 % reduction in the coefficient of friction and a 50.6 % decrease in the specific wear rate. These improvements were attributed to effective load transfer, heterogeneous nucleation, and a free-volume expansion effect, which collectively enhanced strength, ductility, and wear resistance. The combined effect of FPM-BDO and M − WC successfully addressed the major limitations of neat PBT, making these composites promising for automotive, aerospace, and industrial applications that require high-performance, thermally stable, and wear-resistant materials.

1. Introduction

Polymer materials have become indispensable in modern industries because of their lightweight nature, ease of processing, and versatile properties [1,2]. Engineering polymers, such as polyamide [3], polycarbonate [4], and polyethylene terephthalate [5], are widely used in applications ranging from automotive components to electronic devices owing to their excellent thermal, mechanical, and chemical resistance properties. Among them, polybutylene terephthalate (PBT) is preferred for precision applications because of its high mechanical strength, dimensional stability, and chemical resistance [6,7]. Despite these advantages, neat PBT exhibits significant brittleness, which limits its impact resistance and wear performance, particularly under high-stress conditions [8,9]. To overcome these limitations, polymer blending and filler incorporation have been explored as effective strategies [10,11]. However, these conventional approaches often result in performance trade-offs, such as reduced tensile strength, compromised thermal conductivity, or increased brittleness, which restrict their widespread adoption in high-performance applications. In a recent study, Su et al. explored the development of fluorinated graphite (FGr)-reinforced PTFE/PBT composites for deep-sea applications, focusing on enhancing tribological performance under high-pressure seawater conditions. Their findings demonstrated a 96 % reduction in wear rate at optimal FGr content, highlighting the effectiveness of FGr in improving wear resistance and transfer film formation in extreme environments [12].

In this study, a novel PBT composite was developed by incorporating

* Corresponding author. School of Chemical Engineering, Chung-Ang University, Seoul, 06974, Republic of Korea.
E-mail address: jooheonkim@cau.ac.kr (J. Kim).

https://doi.org/10.1016/j.jmrt.2025.04.314
Received 17 March 2025; Received in revised form 29 April 2025; Accepted 29 April 2025
Available online 30 April 2025

functionalized phenolic microsphere (FPM-BDO) and tungsten carbide (WC). The integration of FPM-BDO in a PBT matrix has not been previously reported, highlighting its novelty and potential to offer unique advantages over conventional reinforcement strategies. FPM-BDO acts as a heterogeneous nucleating agent, facilitating crystallization and increasing free volume, which enhances polymer chain mobility. This results in a synergistic improvement in both tensile strength and ductility, mitigating the brittleness commonly observed in neat PBT. Additionally, WC further enhances the tribological and thermal properties of the composite due to its exceptional hardness, high thermal conductivity, and wear resistance [13]. Moreover, WC was modified with 3-mercaptopropyl trimethoxysilane (MPTMS), which improved its interfacial adhesion with the PBT matrix, ensuring enhanced dispersion and stress-transfer efficiency. Previous studies have demonstrated that WC-reinforced polymer composites exhibit enhanced tribological properties in high-wear applications [14,15]. This study builds on those findings by investigating the combined effect of FPM-BDO and MPTMS-modified WC (M − WC) in a PBT matrix.

The final FPM-BDO/M-WC/PBT composite exhibited remarkable improvements across multiple performance metrics. Its tensile strength increased by 20.3 %, reaching 51.21 MPa, while its elongation at break increased 1.94-fold compared to that of neat PBT. The thermal conductivity of the composite improved significantly, reaching 0.627 W/m·K, representing a 129 % increase over that of neat PBT. Additionally, the coefficient of friction decreased by 46.1 %, and the specific wear rate was reduced by 50.6 %, confirming enhanced wear resistance. The combination of FPM-BDO and M − WC effectively mitigated the inherent brittleness of PBT while simultaneously enhancing its mechanical strength, thermal stability, and tribological properties, making the composite a promising material for high-performance industrial applications.

2. Results and discussion

2.1. Characterization of the fillers

The fabrication process of the fillers and composites is schematically illustrated in Fig. 1 and detailed in the experimental section. The morphology of the fillers analyzed using FE-SEM is depicted in Fig. 2. The FE-SEM image of the FPM (Fig. 2a) displayed smooth spherical particles with an average diameter of 3.6 μm, indicating a uniform and well-defined structure. In the case of FPM-BDO, nanosized particles were observed on the surface of the FPM spheres, which increased the particle size to approximately 3.7 μm. As the FPM ratio decreased from 8 % to 2 %, the density of the nanosized particles on the surface increased significantly, resulting in an irregular and rough texture, as shown in Fig. 2b and c. WC exhibited particles featuring an agglomerated structure with sharp edges (Fig. 2d), consistent with its high-hardness properties. However, M − WC exhibited a smooth surface and a uniform particle distribution (Fig. 2e), confirming the success of the surface treatment [16].

The structural characteristics of WC and M − WC were further analyzed using field-emission transmission electron microscopy (FE-TEM), as shown in Fig. 2. The low-resolution TEM image of WC, presented in Fig. 2f, revealed irregularly shaped particles with sharp edges, which is consistent with the agglomerated morphology observed in the FE-SEM images. The lattice fringes were clearly visible, indicating the crystalline nature of WC, and the measured d-spacing of 0.245 nm, corresponded to the characteristic [101] plane of WC, as shown in Fig. 2g. Conversely, the FE-TEM image of M − WC (Fig. 2h) revealed a noticeable change in surface structure, where the particles exhibited a thin, amorphous coating layer due to the MPTMS treatment. Although the lattice fringes of the WC core remained intact, as shown in Fig. 2i, the presence of the coating confirmed the successful surface modification.

The EDS elemental mapping further confirmed the observed surface modifications. The mapping of WC, shown in Fig. 2a, revealed a uniform distribution of tungsten and carbon elements, which are the primary components of WC. The mapping of M − WC (Fig. 2b) displayed additional signals for silicon and sulfur, indicating that an MPTMS coating was present on the WC particles. The clear detection of silicon and sulfur elements confirms the successful chemical modification of the WC surface and the formation of a thin MPTMS layer (see Fig. 3).

The structural and thermal properties of the fillers were analyzed using XRD, FT-IR spectroscopy, and TGA, as shown in Fig. 4. The XRD patterns of WC and M − WC, presented in Fig. 4a, exhibited sharp diffraction peaks, indicating the crystalline nature of WC. Characteristic peaks corresponding to WC were observed at $2\theta = 31.48^{\circ}$, 35.62°, and 48.26°, which are associated with the (001), (100), and (101) planes, respectively. In the case of M − WC, the peak positions remained unchanged, confirming that the MPTMS treatment did not alter the crystalline structure of WC [17].

The FT-IR spectra of the FPM and FPM-BDO were analyzed to confirm the successful chemical modification of the FPM with butanediol. As shown in Fig. 4b, the spectrum of the FPM displayed characteristic peaks at 1595 cm^{-1} and 1476 cm^{-1}, which correspond to the aromatic C═C stretching vibrations and C–H bending vibrations, respectively. Additionally, the broad peak around 3446 cm^{-1} was attributed to the –OH stretching vibrations of the phenolic groups in the FPM [18]. Conversely, the spectrum of FPM-BDO exhibited significant changes. The –OH stretching peak at 3446 cm^{-1} broadened and intensified, confirming the introduction of hydroxyl groups from butanediol. Furthermore, a new peak was observed at 1049 cm^{-1}, which

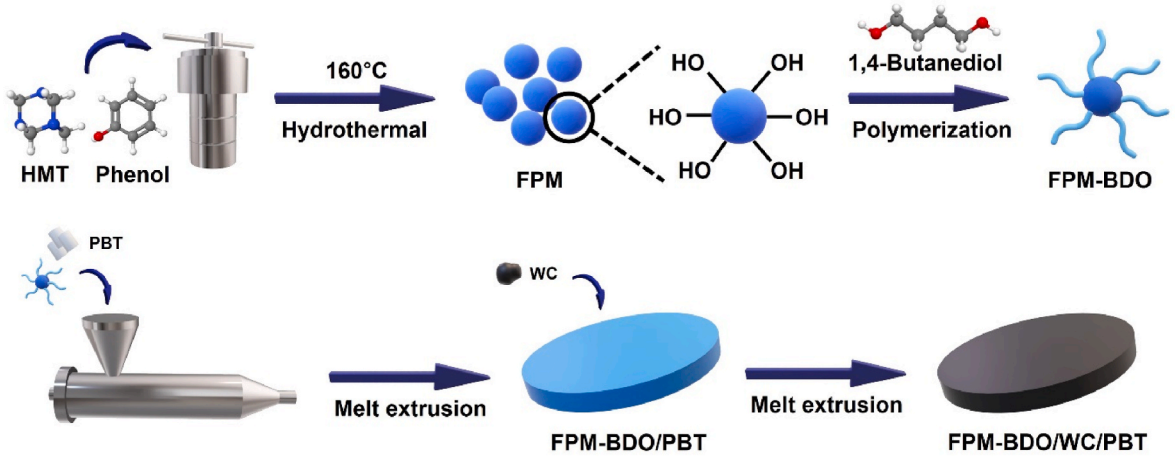

Fig. 1. Schematic illustration of the composite fabrication process.

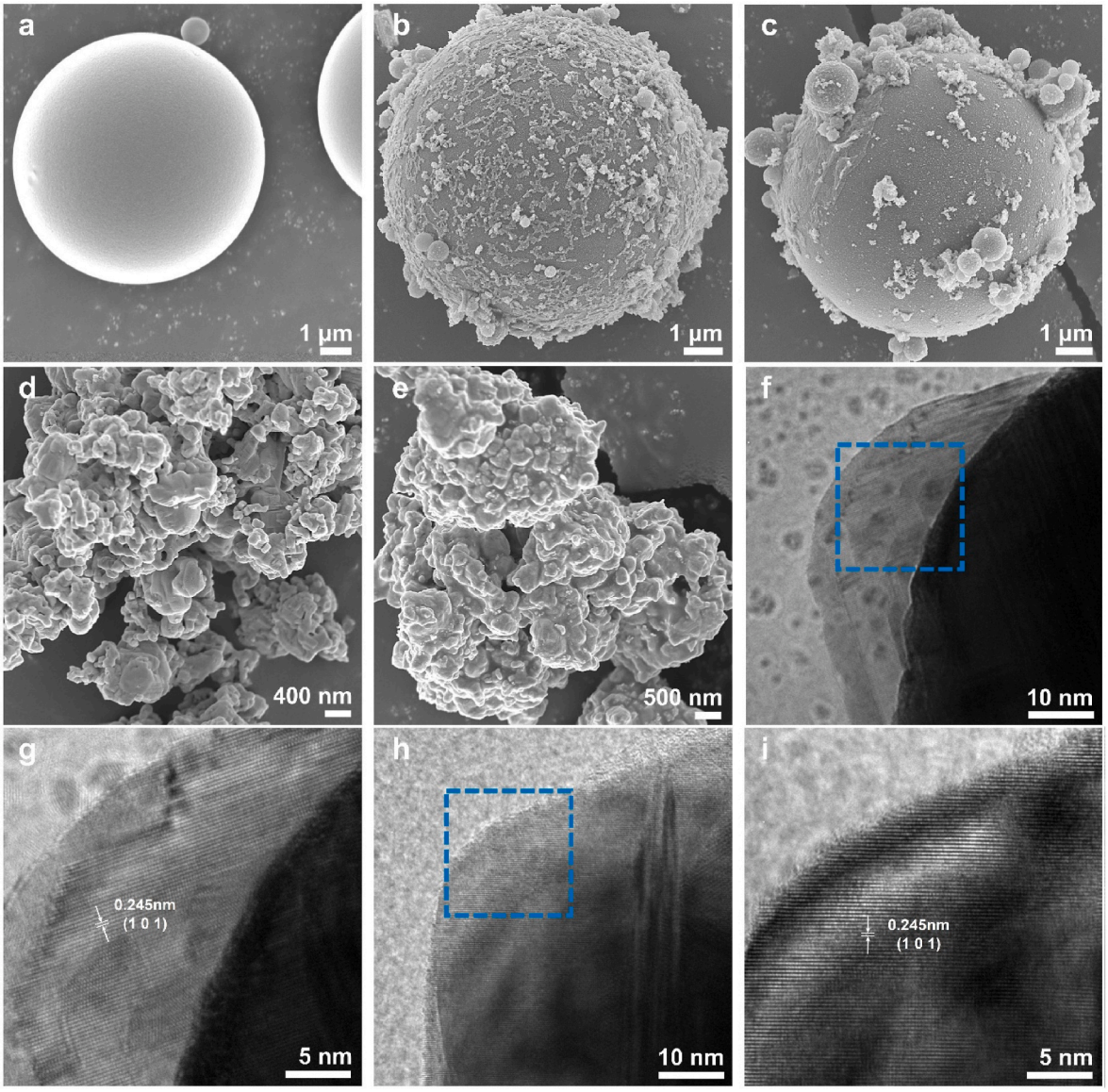

Fig. 2. FE-SEM images of (a) the FPM, (b) FPM-BDO (2 %), (c) FPM-BDO (8 %), (d) WC, and (e) M-WC. (f) Low- and (g) high-resolution FE-TEM images of WC. (h) Low- and (i) high-resolution FE-TEM images of M-WC.

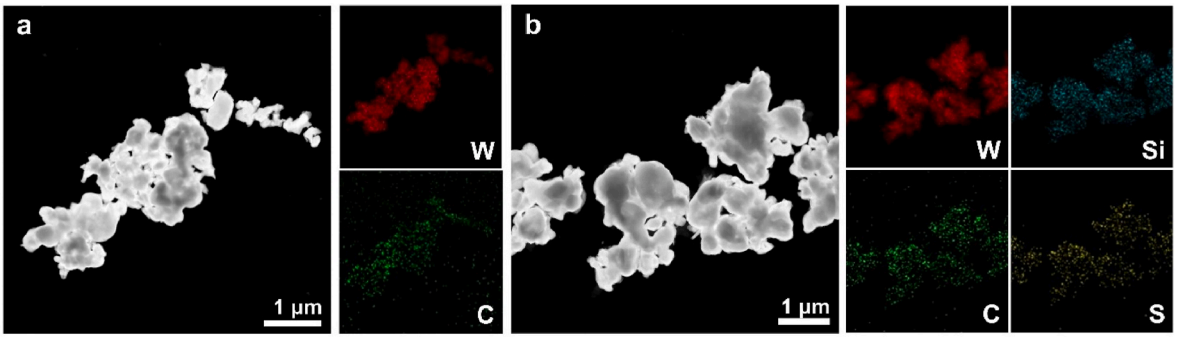

Fig. 3. EDS elemental mappings of (a) WC and (b) M-WC.

corresponds to the C–O stretching vibrations likely originating from newly formed ester bonds due to the reaction with butanediol. Additionally, a distinct peak was detected at 750 cm^{-1}, which is attributed to the out-of-plane bending vibrations of aromatic C–H bonds. This peak, which was absent in the FPM, indicates a change in the substitution pattern of the aromatic ring caused by the grafting of butanediol. These modifications clearly demonstrate that butanediol was successfully grafted onto the FPM, as the characteristic peaks of the FPM were retained while additional peaks unique to butanediol appeared. Similarly, the FT-IR spectra of WC and M − WC (Fig. 4c) displayed no

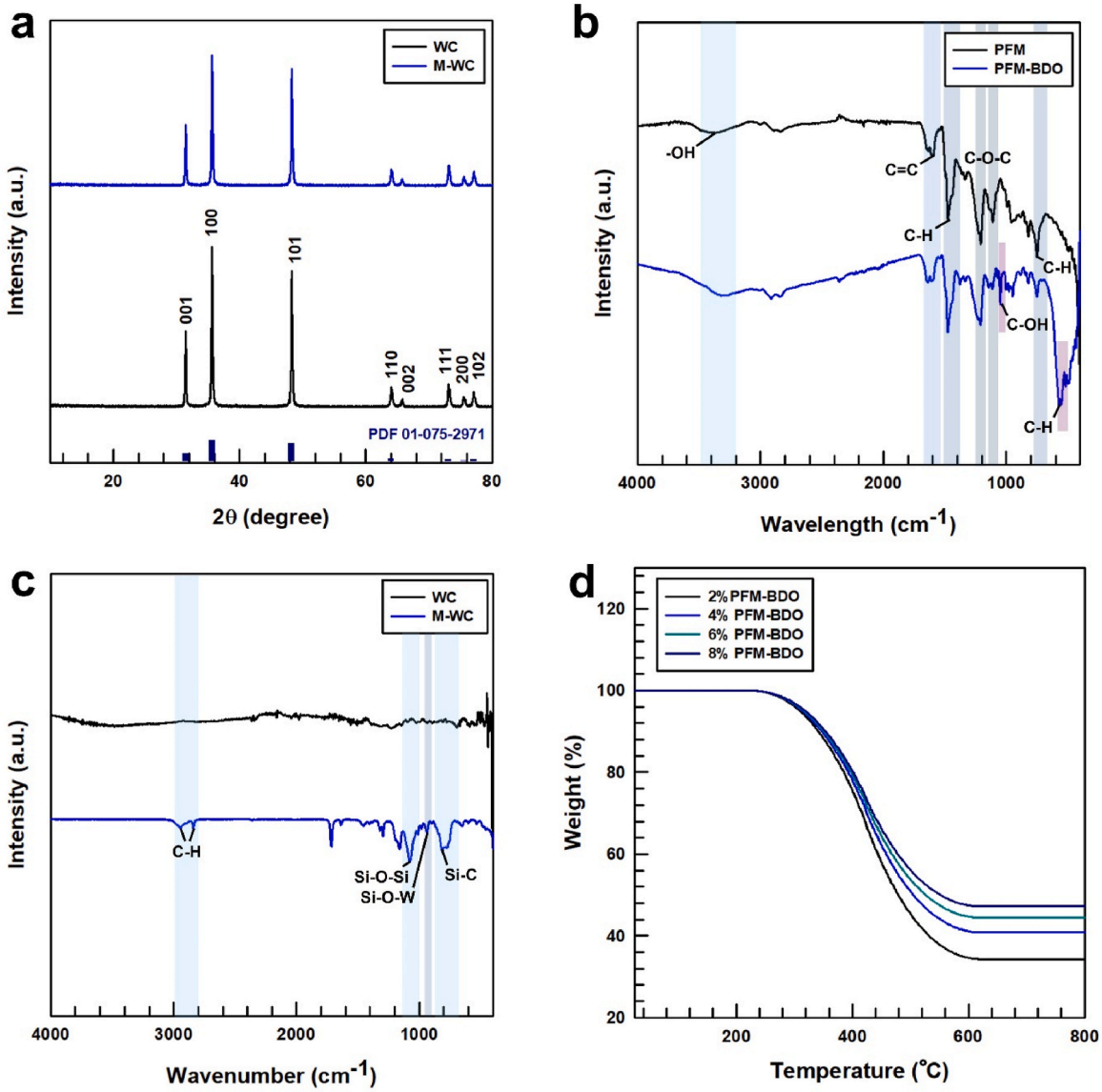

Fig. 4. (a) XRD patterns of WC and M-WC. FT-IR spectra of (b) the FPM and FPM-BDO and (c) WC and M-WC. (d) TGA curves of FPM-BDO.

significant peaks for pristine WC because of its inert nature. However, M − WC exhibited new peaks at 1079 cm^{-1}, 951 cm^{-1}, and 1018 cm^{-1}, corresponding to Si–O–Si, Si–C, and Si–O–W bonds, respectively, confirming the successful attachment of MPTMS onto the WC surface.

The TGA curves of the fillers (Fig. 4d) provided insights into their thermal stability. As the proportion of FPM increased, the thermal stability of the materials improved owing to the relatively stable nature of FPM. The TGA curve of the FPM exhibited an initial weight loss around 300 °C due to the decomposition of residual volatile compounds, followed by a major weight loss between 400 °C and 600 °C due to the degradation of the phenol-formaldehyde framework. Compared to the FPM, FPM-BDO demonstrated slightly higher thermal stability, with its decomposition occurring at a higher temperature, possibly due to the presence of BDO. The TGA curves of WC and M − WC are presented in Fig. S1. WC exhibited no significant weight loss up to 800 °C, reflecting its high thermal stability. M − WC exhibited a slight weight loss around 350 °C, which is attributed to the decomposition of the MPTMS coating.

The XPS spectra of the fillers, shown in Fig. 5, were analyzed to verify the surface chemical composition and successful functionalization of the materials. The C 1s spectrum of the FPM in Fig. 5a displays characteristic peaks at 284.8 eV, 286.2 eV, and 288.6 eV, which correspond to C–C and C═C, C–O, and π→π* shakeup satellites, respectively. The O 1s spectrum in Fig. 5b further confirms the presence of oxygen-containing functional groups, with a peak at 533.2 eV, attributed to C–O bonding. These results confirm the successful synthesis of FPM with functional groups suitable for further chemical modification [19]. Conversely, the spectra of FPM-BDO were observed to exhibit significant changes. The C 1s spectrum in Fig. 5c demonstrates the presence of multiple oxygen-related functional groups, including C–O (286.3 eV), C═O (288.7 eV), and C–O–C (287.5 eV), indicating the successful grafting of butanediol onto the FPM surface. Similarly, the O 1s spectrum in Fig. 5d displays a broad peak with deconvoluted signals, suggesting the formation of C–O–C and C═O bonds, further confirming the modification of the hydroxyl functionality.

The C 1s spectrum of WC in Fig. 5e exhibits a strong peak at 283.5 eV, which is attributed to carbide carbon. The W 4f spectrum in Fig. 5f displays peaks at 31.7 eV and 34.1 eV, confirming the WC chemical state. These results reflect the intrinsic stability and chemical structure of pristine WC [20]. In contrast, M − WC exhibited new peaks due to functionalization with MPTMS. The C 1s spectrum in Fig. 5g illustrates the appearance of a peak at 286.3 eV, which is attributed to C–O bonds introduced by the MPTMS coating. The W 4f spectrum shown in Fig. 5h

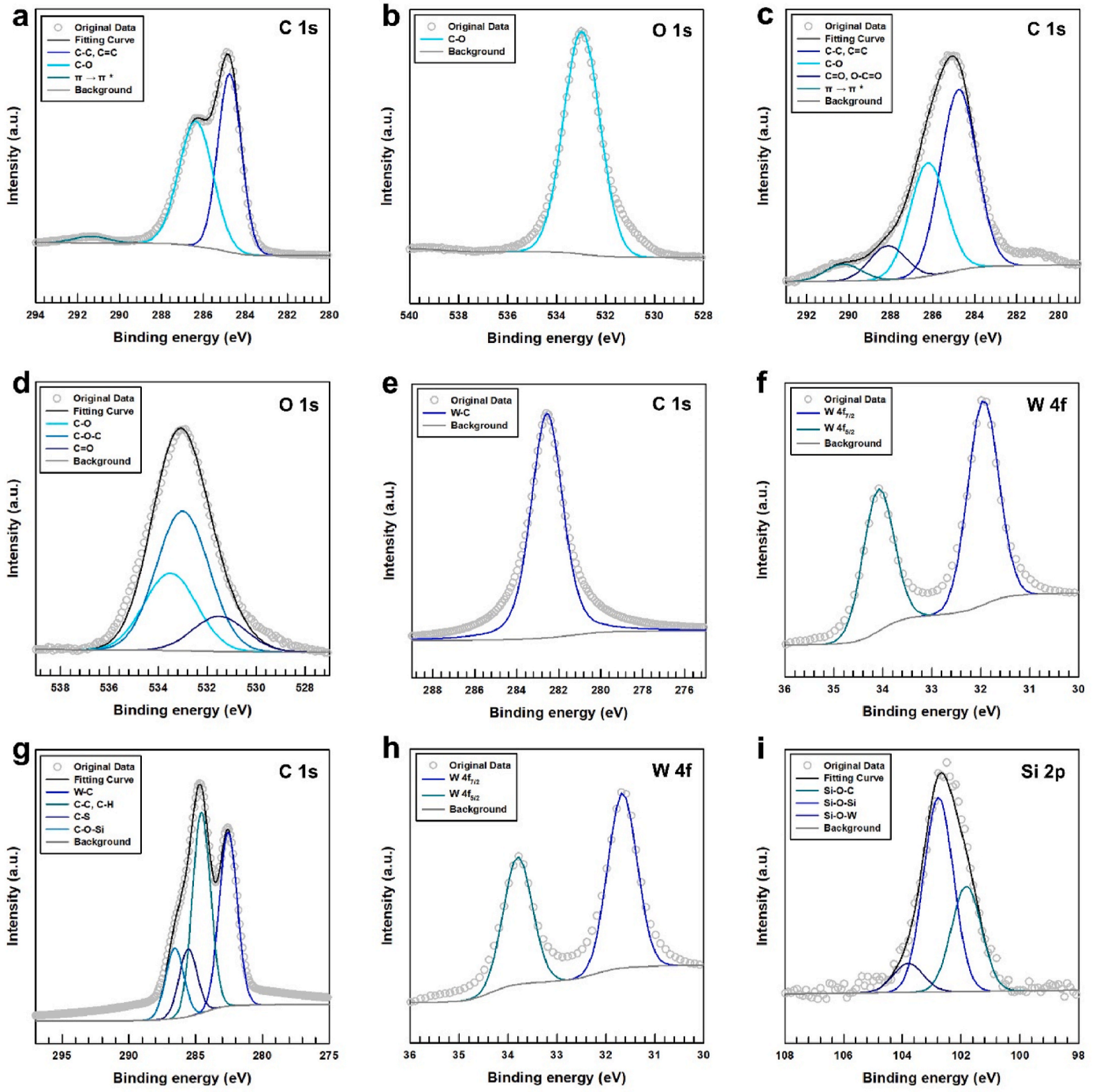

Fig. 5. XPS spectra of (a) FPM C 1s, (b) FPM O 1s, (c) FPM-BDO C 1s, (d) FPM-BDO O 1s, (e) WC C 1s, (f) WC W 4f, (g) M − WC C 1s, (h) M − WC W 4f, and (i) M − WC Si 2p.

remained largely unchanged, with WC peaks still dominant. Furthermore, the Si 2p spectrum (Fig. 5i) displays distinct peaks at 102.3 eV and 103.5 eV, which correspond to Si–O–Si and Si–O–W bonds, respectively. This verifies that MPTMS has been successfully attached to the WC surface.

2.2. Cross-sectional morphologies of composites

The cross-sectional morphologies of neat PBT and the various FPM-BDO/PBT and FPM-BDO/M-WC/PBT composites were analyzed using FE-SEM, and the results are shown in Fig. 6. Neat PBT exhibited a smooth and homogeneous structure, as revealed by its cross-sectional image in Fig. 6a. Conversely, the FPM-BDO/PBT composites exhibited significant structural modifications depending on the FPM-BDO content. For 2FPM-BDO/PBT, its cross-section (Fig. 6b) displayed a microfibrillar structure, indicating enhanced ductility. As the FPM-BDO content increased to 4 % and 6 % (Fig. 6c and d), a denser microfibrillar network formed, contributing to improved load transfer between the filler and polymer matrix [21]. However, at 8 % FPM-BDO/PBT (Fig. 6e), particle aggregation was observed, leading to localized filler clustering, which may diminish the mechanical properties due to stress concentration effects [22].

For the FPM-BDO/M-WC/PBT composites, the addition of M − WC further influenced the cross-sectional morphology. The cross-section of

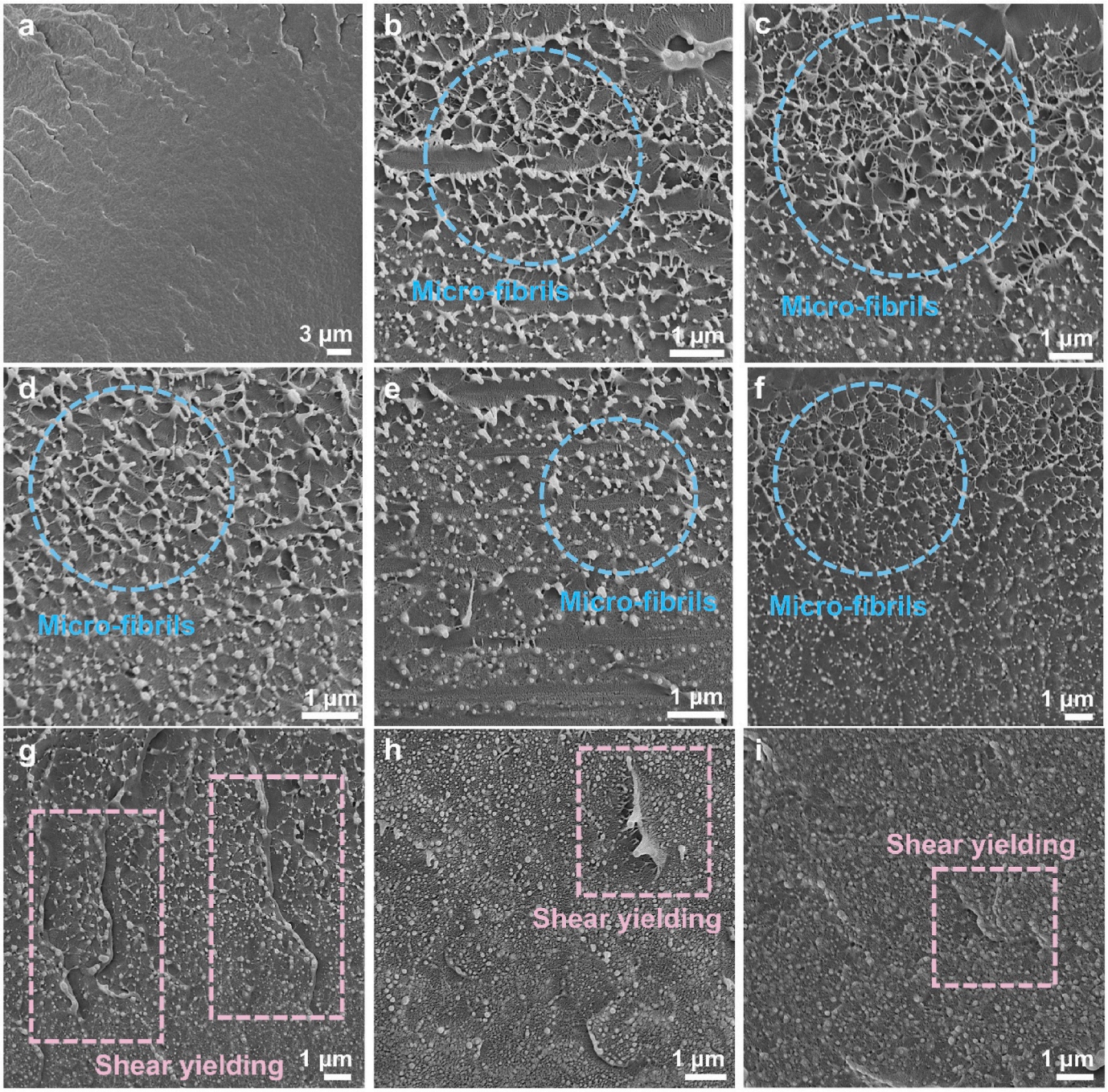

Fig. 6. Cross-sectional FE-SEM images of (a) neat PBT, (b) 2FPM-BDO/PBT, (c) 4FPM-BDO/PBT, (d) 6FPM-BDO/PBT, (e) 8FPM-BDO/PBT, (f) 4FPM-BDO/10M-WC/PBT, (g) 4FPM-BDO/20M-WC/PBT, (h) 4FPM-BDO/30M-WC/PBT, and (i) 4FPM-BDO/40M-WC/PBT.

4FPM-BDO/10M-WC/PBT (Fig. 6f) exhibited a uniform distribution of M − WC particles alongside FPM-BDO, indicating good dispersion and interaction with the matrix. At a 20 % M − WC content, shown in Fig. 6g, a dense distribution of M − WC particles was observed, accompanied by shear yielding features, suggesting enhanced mechanical toughness. At a 30 % M − WC content, (Fig. 6h), the composite displayed both microfibrillation and shear yielding, ensuring balanced structural reinforcement [23]. However, at the highest filler content, the microfibrillar structure was no longer observed. Instead, the material exhibited shear yielding as the dominant deformation mechanism, indicating that at this high filler concentration, the reinforcing effect of microfibrils was suppressed in favor of plastic deformation.

2.3. Thermal properties of the composites

Fig. 7 illustrates the thermal properties of neat PBT and the various FPM-BDO/PBT and FPM-BDO/M-WC/PBT composites analyzed using DSC, TGA, and thermal conductivity measurements. The DSC curves of the composites are presented in Fig. 7a, while the corresponding T_g and T_{cc} values are summarized in Fig. 7b. According to the DSC analysis, Neat PBT exhibited a single endothermic melting peak, whereas the FPM-BDO/PBT composites displayed a double melting peak in their DSC curves. This double melting behavior is typically associated with recrystallization processes or the presence of different crystal structures within the polymer matrix. The introduction of FPM-BDO fillers altered the crystallization behavior, leading to a lower T_{cc}, which suggests an

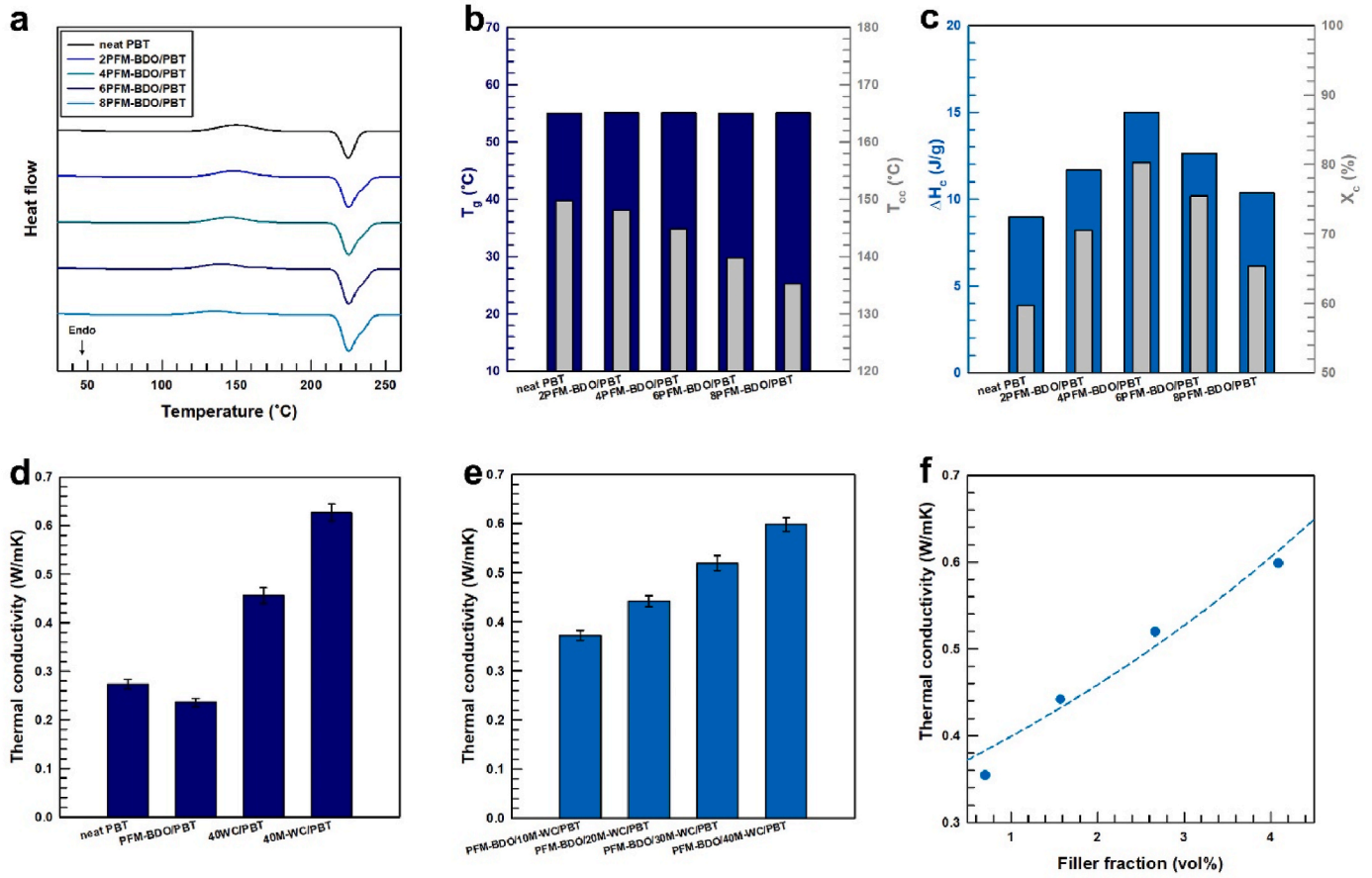

Fig. 7. (a) DSC curves, (b) T_g and T_{cc} values, and (c) ΔH_c and X_c values of the composites. (d) Thermal conductivity of the reference composites and (e) the composites with different filler ratios. (f) Theoretical thermal conductivity values obtained using the Agari–Uno model.

enhancement in nucleation due to the presence of the fillers [24]. The cold crystallization temperature (Tcc) represents the temperature at which polymer chains reorganize into crystalline domains during reheating. A lower Tcc indicates enhanced nucleation efficiency and improved chain mobility, leading to easier crystallization. The incorporation of heterogeneous nucleating agents, such as FPM-BDO, introduces abundant nucleation sites within the polymer matrix, thereby lowering the energy barrier for crystallization. These agents promote crystallization through both chemical interactions (e.g., hydrogen bonding, dipole-dipole interactions) and epitaxial nucleation mechanisms, enabling the polymer chains to crystallize at lower temperatures [25].

Among the composites, 8FPM-BDO/PBT exhibited the lowest T_{cc} and a relatively high degree of crystallinity (Xc), confirming that FPM-BDO effectively acted as a heterogeneous nucleating agent by providing abundant nucleation sites, thereby promoting crystallization [26].

The thermal conductivity of the composites is shown in Fig. 7e, while the theoretical values obtained from the Agari–Uno model are presented in Fig. 7f. Neat PBT exhibited the lowest thermal conductivity (0.273 W/m·K), while the incorporation of FPM-BDO alone slightly reduced the thermal conductivity to 0.236 W/m·K. This decrease can be attributed to the low intrinsic thermal conductivity of FPM-BDO, which introduces additional interfacial boundaries and increases the free volume within the matrix, thereby hindering efficient phonon transport [27].

In contrast, the addition of WC significantly improved the thermal conductivity due to its inherently high thermal conductivity and its ability to form continuous heat conduction pathways. FPM-BDO/10M-WC/PBT, 20M-WC/PBT, and 30M-WC/PBT exhibited a steady increase in thermal conductivity, with FPM-BDO/40M-WC/PBT reaching the highest value (0.5987 W/m·K). However, the difference in thermal conductivity between 30M − WC and 40M − WC was relatively small, indicating that the percolation threshold was reached at 30 wt%, and further addition of WC resulted in only marginal improvement due to slight filler aggregation [28].

The MPTMS surface modification of WC played a critical role in enhancing interfacial compatibility, reducing interfacial thermal resistance, and ensuring efficient phonon transport. The experimental values closely matched the predictions from the Agari–Uno model (Fig. 7f), confirming its applicability in predicting the thermal transport behavior of these composites. To further verify the experimental results, the Agari–Uno model was employed to predict the thermal transport behavior of the composites (Fig. S3). A more detailed theoretical approach regarding the calculation of composite thermal conductivity using the Agari–Uno model, including derivations and parameters used, is provided in the Supporting Information.

2.4. Mechanical properties of composites

The stress–strain curves of neat PBT and the FPM-BDO/PBT composites are presented in Fig. 8a, while the corresponding tensile strength and elongation at break values are summarized in Fig. 8b. Neat PBT exhibited a tensile strength of 49.82 MPa and an elongation at break of 10.7 %, indicative of its inherent brittleness [29]. The incorporation of FPM-BDO fillers enhanced the tensile strength and ductility, with the most significant improvement observed in 6FPM-BDO/PBT, which achieved a tensile strength of 51.21 MPa and an elongation of 18.2 %. This improvement suggests that FPM-BDO acts as a stress-transfer agent, facilitating load distribution within the polymer matrix. However, at 8 wt% FPM-BDO, both tensile strength and elongation decreased to 48.30 MPa and 14.7 %, respectively, likely due to filler aggregation and

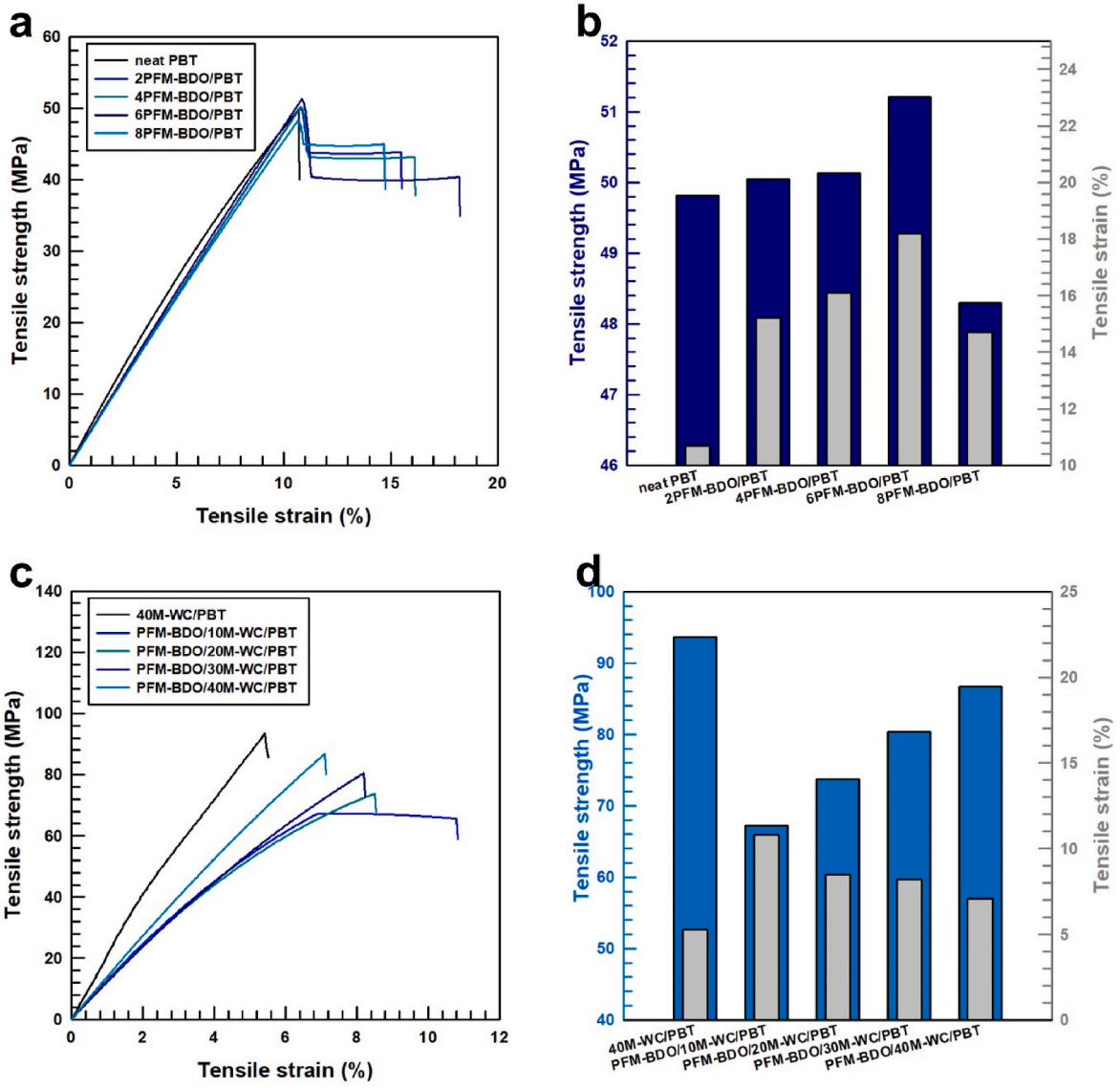

Fig. 8. (a) Stress–strain curves of the composites. (b) Tensile strength and strain of the composites with various FPM-BDO ratios. (c) Stress–strain curves of the composites with different M − WC filler ratios. (d) Tensile strength and strain of the composites with different M − WC filler ratios.

microvoid formation, leading to a reduction in interfacial adhesion and mechanical stability.

The stress–strain behavior of FPM-BDO/M-WC/PBT composites is depicted in Fig. 8c, with the tensile strength and elongation values summarized in Fig. 8d. The addition of M − WC significantly enhanced the tensile strength, attributed to the inherent stiffness and mechanical reinforcement of tungsten carbide. The 40M-WC/PBT composite exhibited the highest tensile strength of 93.6 MPa, but its elongation was limited to 5.3 %, indicative of increased brittleness at high filler content. Among the FPM-BDO/M-WC/PBT composites, FPM-BDO/30M-WC/PBT displayed the best balance between strength and ductility, achieving a tensile strength of 80.4 MPa and an elongation of 8.2 %. This suggests that 30 wt% M − WC provides optimal reinforcement, efficiently transferring stress without excessive particle agglomeration. However, at 40 wt% M − WC, the tensile strain decreased to 7.1 %, suggesting that increased filler content led to reduced flexibility due to more rigid particle interactions.

The mechanical reinforcement observed in the FPM-BDO/PBT and FPM-BDO/M-WC/PBT composites can be attributed to multiple reinforcing mechanisms. First, the uniform dispersion of FPM-BDO fillers within the PBT matrix facilitates stress transfer across the polymer chains, improving load distribution and reducing stress concentrations. The increased elongation at break observed at moderate FPM-BDO content (4–6 wt%) suggests that these fillers act as micro-reinforcement sites, preventing crack propagation and delaying fracture.

In contrast, the incorporation of M − WC significantly improves the stiffness of the composites due to the inherent rigidity of tungsten carbide [30]. At moderate filler content (10–30 wt% M − WC), the increased tensile strength indicates effective stress transfer between the matrix and the filler. However, at higher M − WC concentrations, filler aggregation reduces the efficiency of stress transfer and increases the likelihood of brittle fracture due to localized stress concentrations.

Additionally, fracture surface analysis (Fig. S6) suggests that multiple toughening mechanisms contribute to the observed improvements. In the FPM-BDO/PBT composites, the presence of microfibrils and shear yielding features indicates enhanced energy dissipation during deformation. This suggests that FPM-BDO enhances the plastic deformation capacity of the polymer, increasing its ductility. Conversely, in the M-WC-containing composites, the presence of microcracks and interfacial debonding suggests that WC reinforcement primarily enhances the material's stiffness, leading to a more brittle fracture behavior at high filler content.

Overall, these findings suggest that the combination of FPM-BDO and M − WC fillers can be optimized to achieve a balance between strength and toughness in PBT composites. The synergistic effect of FPM-BDO in improving ductility and M − WC in enhancing stiffness provides an effective strategy for tuning the mechanical properties of polymer composites. However, excessive filler content in both cases leads to diminishing returns due to filler aggregation and stress localization, emphasizing the need for controlled dispersion to achieve optimal mechanical performance.

The mechanism by which FPM-BDO enhances the ductility of the PBT matrix is illustrated in Fig. 9. The brittle fracture behavior of neat PBT is primarily attributed to its rigid molecular chain structure and strong intermolecular interactions. These factors restrict the movement and rotation of the PBT molecular chains, leading to limited chain mobility and poor energy dissipation under mechanical stress. This results in a brittle fracture with minimal elongation before failure [31].

The hydroxyl groups in the FPM-BDO fillers establish hydrogen-bonding interactions with the carbonyl groups in the PBT backbone. These interactions effectively act as stress-transfer bridges, improving the load distribution and reducing local stress concentration within the matrix. Additionally, the multiarmed architecture of FPM-BDO further enhances ductility by creating localized regions with increased free volume. These regions act as molecular "cushions," enabling increased chain mobility and reducing the likelihood of brittle fracture. Simultaneously, the hydrogen-bonding interactions ensure that the overall mechanical integrity of the composite is preserved, even under high strain. This dual functionality of FPM-BDO—serving as both a reinforcement agent and a ductility enhancer—results in simultaneous strengthening and toughening of the PBT matrix.

2.5. Tribological properties of composites

The tribological properties of neat PBT and its composites containing unmodified WC and M − WC were analyzed through friction coefficient and specific wear rate measurements, as shown in Fig. 10. The friction coefficient results (Fig. 10a) indicate that neat PBT exhibited a relatively high friction coefficient (0.3459), which can be attributed to its inherent surface roughness and high resistance during sliding [32]. The incorporation of unmodified WC (40WC/PBT) into the PBT matrix resulted in a reduced friction coefficient (0.3875), corresponding to a 12.7 % improvement compared to neat PBT. This reduction can be explained by the high hardness of WC, which serves as a protective barrier, reducing direct contact between the polymer surface and the counterpart material, thereby minimizing friction-induced wear. However, unmodified WC exhibited weak interfacial adhesion with the polymer matrix, which can lead to nonuniform load distribution and partial WC detachment under frictional stress.

In contrast, the MPTMS-treated WC (M − WC) composites showed a more pronounced reduction in the friction coefficient due to the enhanced interfacial bonding and uniform dispersion of WC particles [33]. Specifically, the 40M-WC/PBT composite exhibited the lowest friction coefficient (0.3078), representing an 11.3 % improvement over unmodified WC/PBT and a 19.7 % improvement over neat PBT. The MPTMS treatment improves interfacial adhesion, preventing particle pull-out and ensuring a more stable contact surface, leading to reduced frictional resistance. Additionally, the functionalized WC surface minimizes micro-roughness, further lowering the friction coefficient.

The specific wear rate (Ws) was calculated using the following equation:

$$W_s = \frac{wear\ loss}{D \times F \times L}$$

where D, F, and L denote the density of the composite, the applied load, and the sliding distance, respectively. The physical parameters utilized for these calculations are summarized in Table 1. The specific wear rate results, as illustrated in Fig. 10b, validate the effectiveness of M − WC in improving wear resistance. Neat PBT exhibited the highest specific wear rate (5.2469×10^{-4} $mm^3/N{\cdot}m$), demonstrating its susceptibility to surface degradation under prolonged frictional stress. The addition of unmodified WC led to a decrease in the wear rate (3.1299×10^{-4} $mm^3/N{\cdot}m$), corresponding to a 40.3 % improvement, primarily due to the hardness of WC providing better resistance to abrasion. However, the weak interfacial bonding between unmodified WC and PBT limits its effectiveness, leading to localized stress concentrations and particle

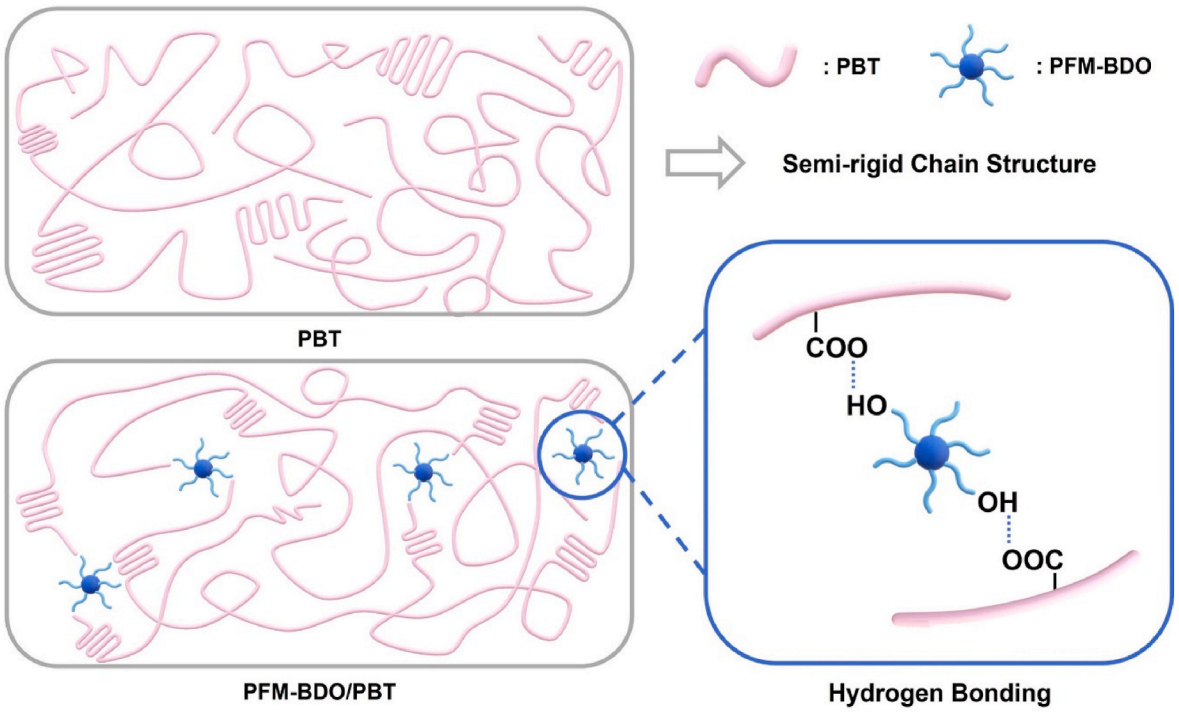

Fig. 9. Ductility-enhancing mechanism of the FPM-BDO/PBT composites.

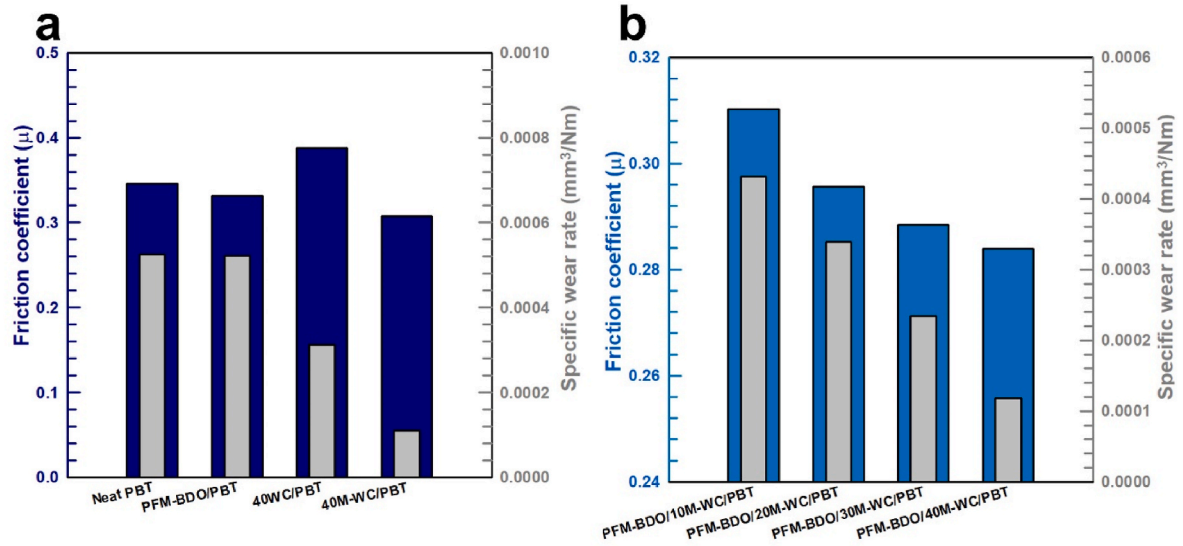

Fig. 10. (a) Friction coefficients and specific wear rates of (a) the reference composites and (b) the composites with various filler ratios.

Table 1
Physical properties of the composites before and after the wear test.

Sample	Density (g/cm^3)	Before weight (g)	After weight (g)	Weight difference (g)	Applied load (N)	Sliding distance (m)
Neat PBT	1.35	3.5929	3.5878	0.0051	10	720
FPM-BDO/PBT	1.33	3.4168	3.4118	0.0050		
40WC/PBT	2.13	4.3325	4.3277	0.0048		
40M-WC/PBT	2.13	4.3951	4.3934	0.0017		
FPM-BDO/10M-WC/PBT	1.48	3.8702	3.8656	0.0046		
FPM-BDO/20M-WC/PBT	1.64	3.9708	3.9668	0.0040		
FPM-BDO/30M-WC/PBT	1.84	4.1431	4.1400	0.0031		
FPM-BDO/40M-WC/PBT	2.11	4.2234	4.2216	0.0018		

pull-out, which can contribute to long-term material wear.

The M-WC-based composites demonstrated further improvements in wear resistance. 10 % M-WC/PBT exhibited a reduced wear rate of 4.3168×10^{-4} mm^3/N·m, indicating an initial enhancement in wear resistance. 20 % M-WC/PBT exhibited a wear rate of 3.3875×10^{-4} mm^3/N·m, suggesting a more effective load transfer due to improved interfacial bonding. 30 % M-WC/PBT achieved a wear rate of 2.3400×10^{-4} mm^3/N·m, highlighting an optimal balance between load distribution and wear resistance. 40 % M-WC/PBT exhibited the lowest wear rate of 1.1848×10^{-4} mm^3/N·m, representing an overall improvement of 77.4 % over neat PBT and 62.1 % over unmodified WC/PBT.

The enhanced wear resistance of M-WC-based composites is attributed to their strong interfacial adhesion and uniform filler dispersion, which promote effective load transfer and prevent WC particle detachment. This finding suggests that MPTMS treatment not only strengthens the filler-polymer interface but also ensures a homogeneous stress distribution, reducing material loss and enhancing long-term durability [34].

The FE-SEM images of the composite surfaces after the wear test are presented in Fig. 11. These images provide crucial insights into the wear mechanisms of the neat PBT and PBT-based composites, highlighting differences in material removal, surface roughness, and filler-matrix interactions.

The worn surface of neat PBT (Fig. 11a) exhibits deep, irregular wear tracks, indicating severe adhesive wear. The polymer matrix undergoes extensive plastic deformation and material removal, resulting in rough, uneven wear surfaces. The absence of reinforcement fillers leads to localized stress concentration, causing excessive surface damage under frictional stress [35]. The significant deformation observed further confirms that neat PBT lacks sufficient resistance to sliding wear.

In contrast, the worn surface of FPM-BDO/WC/PBT (Fig. 11b) demonstrates a reduction in wear severity, with relatively smoother wear tracks compared to neat PBT. The incorporation of WC particles improves stress distribution, minimizing severe surface degradation. However, due to weak interfacial adhesion between unmodified WC and the polymer matrix, some WC particles are detached from the wear track, indicating that unmodified WC offers limited reinforcement due to insufficient bonding with PBT.

The FPM-BDO/10M-WC/PBT composite (Fig. 11c) shows shallow and uniform wear tracks, indicating effective wear resistance enhancement due to the MPTMS treatment on WC. The improved interfacial adhesion between M − WC and PBT prevents particle detachment and enhances stress transfer during sliding wear. The smoother wear tracks suggest that the composite structure remained stable under frictional stress, with minimal material loss.

As the M − WC content increases, the worn surfaces exhibit progressively less damage and better surface integrity. The FPM-BDO/20M-WC/PBT (Fig. 11d) and FPM-BDO/30M-WC/PBT (Fig. 11e) composites exhibit minimal material removal, with a more continuous and uniform surface morphology. The presence of M − WC particles enhances load distribution, significantly reducing the depth and width of wear tracks. The nearly uniform height of the worn and unworn regions suggests greatly reduced material loss, confirming the protective effect of well-dispersed M − WC fillers.

The FPM-BDO/40M-WC/PBT composite (Fig. 11f) demonstrates the highest wear resistance, with its worn surface exhibiting exceptionally smooth and uniform wear tracks. The absence of visible surface damage or particle detachment suggests that the strong interfacial adhesion between M − WC and PBT ensures structural stability during extended wear cycles. The high thermal and mechanical stability of M − WC,

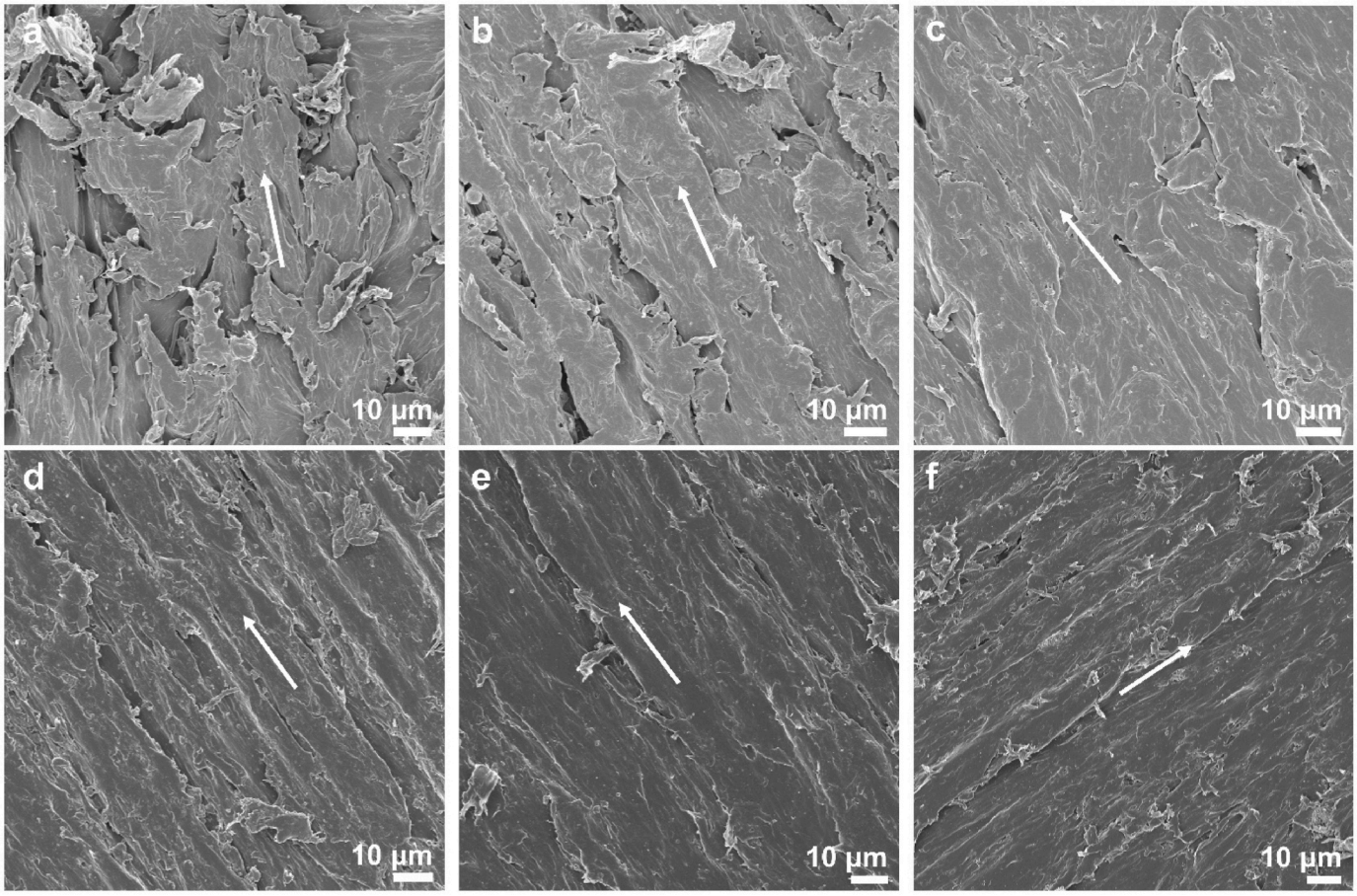

Fig. 11. FE-SEM images of (a) neat PBT, (b) FPM-BDO/WC/PBT, (c) FPM-BDO/10M-WC/PBT, (d) FPM-BDO/20M-WC/PBT, (e) FPM-BDO/30M-WC/PBT, and (f) FPM-BDO/40M-WC/PBT composites after the wear test.

confirmed by TGA results, allows it to withstand prolonged frictional stress without degradation.

To further analyze wear mechanisms, Fig. S4 presents high-magnification SEM images of the worn composite surfaces. The worn region of neat PBT (Fig. S4a) displays severe plastic deformation, deep grooves, and micro-cracks, confirming that adhesive wear is the dominant wear mechanism. In contrast, FPM-BDO/40M-WC/PBT (Fig. S4b) exhibits shallow grooves and a well-maintained surface, indicating a transition from severe adhesive wear to mild abrasive wear, due to the presence of hard M − WC particles enhancing wear resistance.

Further confirmation of wear behavior is provided in Fig. S5, which shows SEM images of the wear test ball surfaces after friction testing. The ball surfaces tested against neat PBT (Fig. S5a) exhibit significant material transfer and deep wear scars, indicating high friction and severe wear interactions. However, as the M − WC content increases, the wear scars become progressively shallower and more uniform (Fig. S5b–f), confirming that M − WC reinforcement reduces direct material transfer and enhances composite durability.

3. Conclusions

In this study, a novel FPM-BDO/M-WC/PBT composite was developed to enhance mechanical strength, thermal conductivity, and wear resistance while addressing the inherent brittleness of neat PBT. The incorporation of FPM-BDO facilitated heterogeneous nucleation and increased free volume, thereby improving crystallization behavior and ductility. Additionally, M − WC, with its high hardness and thermal conductivity, significantly enhanced wear resistance and thermal stability while maintaining strong interfacial adhesion with the PBT matrix. The optimized FPM-BDO/M-WC/PBT composite exhibited a 20.3 % higher tensile strength of 51.21 MPa and a 1.94-fold greater elongation at break than neat PBT. Its thermal conductivity increased to 0.627 W/m·K, a 129 % enhancement compared to that of neat PBT. Additionally, its coefficient of friction decreased by 46.1 %, and its specific wear rate was reduced by 50.6 %, confirming superior tribological performance. FE-SEM analysis of the worn surfaces revealed smooth wear tracks and reduced material detachment, highlighting the effectiveness of M − WC in reinforcing the durability of the composite under frictional conditions. Overall, the integration of FPM-BDO and M − WC successfully improved the thermal, mechanical, and wear-resistance properties of PBT composites, making them promising candidates for automotive, aerospace, and industrial applications that require high-performance, thermally stable, and wear-resistant materials.

Declaration of competing interest

The authors declare that they have no known competing financial interests or personal relationships that could have appeared to influence the work reported in this paper.

Acknowledgments

This work was supported by Korea Institute of Energy Technology Evaluation and Planning (KETEP) grant funded by the Korea government (MOTIE) RS-2024-00398346, ESS BigData-Based O&M and Asset Management Technical Manpower Training) and the National Research Foundation of Korea (NRF) grant funded by the Korea government

(MSIT) (NRF-2022M3H4A1A02076956).

Appendix A. Supplementary data

Supplementary data to this article can be found online at https://doi.org/10.1016/j.jmrt.2025.04.314.

References

[1] Yu Q, Tian Z, Li G, Yang Y, Chen X, Wang D, et al. Multifunctional composite capsules in drug delivery systems: bridging pharmaceutical and biomedical applications. Adv Compos Hybrid Mater 2025;8. https://doi.org/10.1007/s42114-024-01203-y.

[2] Prashanth Palani Velayuda Shanmugasundram H, Jayamani E, Soon KH. Review: classification, theories, and methodologies concerning bio-based polymer dielectric composites. Renew Sustain Energy Rev 2025;209. https://doi.org/10.1016/j.rser.2024.115026.

[3] Gkaliou K, Ørsnæs MV, Holm AH, Daugaard AE. Accelerated hydrolytic degradation of glass fiber-polyamide (PA66) composites. Polym Degrad Stabil 2025;234. https://doi.org/10.1016/j.polymdegradstab.2025.111256.

[4] Soliman OR, Mabied AF, Ibrahim SA, Labeeb AM. Nanosilica/recycled polycarbonate composites for electronic packaging. Mater Chem Phys 2025;329. https://doi.org/10.1016/j.matchemphys.2024.130105.

[5] Poonia K, Sonu Singh P, Ahamad T, Nguyen VH, Katin KP, et al. Transforming waste polyethylene terephthalate (PET) into high-performance activated carbon-supported composites for pollutant degradation: a synergy of experiments and DFT insights. Carbon N Y 2025;234. https://doi.org/10.1016/j.carbon.2025.120001.

[6] Dutta K, Duarah R, Purbey R, Jayaramudu J, Das MR. Development of biodegradable high-alumina clay-modified poly (butylene adipate-Co-terephthalate) composites for sustainable packaging applications. J Appl Polym Sci 2025. https://doi.org/10.1002/app.56680.

[7] Tabaka W, Schartel B. Less is more: optimised fire performance in glass fibre-reinforced polybutylene terephthalate laminates with concentrated flame retardant top layer. Composites Part C: Open Access 2025:100577. https://doi.org/10.1016/j.jcomc.2025.100577.

[8] Qin S, Guo Z, Wu Z, Yuan C. Insights of particle types on interface wear properties of different water-lubricated bearing materials. Tribol Int 2024;200. https://doi.org/10.1016/j.triboint.2024.110140.

[9] Nam D, Lee G, Kim J. Effect of phosphorus vacancies on activity of Fe-doped Nickel phosphide by NaBH4 reduction for efficient oxygen evolution under alkaline conditions. J Ind Eng Chem 2023;123:201–8. https://doi.org/10.1016/j.jiec.2023.03.035.

[10] Vyavahare SA, Kharat BM, More AP. Polybutylene terephthalate (PBT) blends and composites: a review. Vietnam Journal of Chemistry 2024. https://doi.org/10.1002/vjch.202300177.

[11] Tuba Özdemir GE, Mecit GE. Prediction of tribological properties of PC-PBT/GNP-MWCNT nanocomposites using machine learning models. J Appl Polym Sci 2025. https://doi.org/10.1002/app.56834.

[12] Su Q, Wang Z, Liu L, Wang H, Wang J, Wang Y, et al. Fluorinated graphite reinforced polytetrafluoroethylene/poly(butylene terephthalate) composites as friction materials for deep-sea applications. J Appl Polym Sci 2024;141. https://doi.org/10.1002/app.55645.

[13] Li Z, Zou Q, Li Y, Wang M, Gu H, Yin Y, et al. Effects of TaCx on the microstructure and properties of WC composites. J Eur Ceram Soc 2024;44:7451–64. https://doi.org/10.1016/j.jeurceramsoc.2024.05.017.

[14] Chen L, Lan Y, Cheng Y, Zeng J, Ma Y, Yu S, et al. Friction behavior and wear mechanism of laser cladded FeNiCr-WC composite coatings in comparison with different friction pairs. J Mater Res Technol 2024;31:1956–73. https://doi.org/10.1016/j.jmrt.2024.06.206.

[15] Da Q, jie Kang J, zheng Ma G, kuan Zhou Y, Fu Z qiang, Zhu L na, et al. Research on microstructure, mechanical property and wear mechanism of AlCoCrFeNi/WC composite coating fabricated by HVOF. Tribol Int 2024;200. https://doi.org/10.1016/j.triboint.2024.110149.

[16] Xavier JR. Superior surface protection, mechanical and hydrophobic properties of silanized tungsten carbide nanoparticles encapsulated epoxy nanocomposite coated steel structures in marine environment. Silicon 2022;14:11147–61. https://doi.org/10.1007/s12633-022-01842-0.

[17] Sagadevan S, Das I, Singh P, Podder J. Synthesis of tungsten carbide nanoparticles by hydrothermal method and its Characterization. J Mater Sci Mater Electron 2017;28:1136–41. https://doi.org/10.1007/s10854-016-5638-3.

[18] Guo SR, Gong JY, Jiang P, Wu M, Lu Y, Yu SH. Biocompatible, luminescent Silver@Phenol formaldehyde resin core/shell nanospheres: large-scale synthesis and application for in vivo bioimaging. Adv Funct Mater 2008;18:872–9. https://doi.org/10.1002/adfm.200701440.

[19] Yu Y, Xu P, Chang M, Chang J. Aging properties of phenol-formaldehyde resin modified by bio-oil using UV weathering. Polymers 2018;10. https://doi.org/10.3390/polym10111183.

[20] Krasovskii PV, Malinovskaya OS, Samokhin AV, Blagoveshchenskiy YV, Kazakov VA, Ashmarin AA. XPS study of surface chemistry of tungsten carbides nanopowdersproduced through DC thermal plasma/hydrogen annealing process. Appl Surf Sci 2015;339:46–54. https://doi.org/10.1016/j.apsusc.2015.02.152.

[21] Zhao J, Wang G, Chai J, Chang E, Wang S, Zhang A, et al. Polylactic acid/UV-crosslinked in-situ ethylene-propylene-diene terpolymer nanofibril composites with outstanding mechanical and foaming performance. Chem Eng J 2022;447. https://doi.org/10.1016/j.cej.2022.137509.

[22] Sun X, Kharbas H, Peng J, Turng LS. A novel method of producing lightweight microcellular injection molded parts with improved ductility and toughness. Polymer (Guildf) 2015;56:102–10. https://doi.org/10.1016/j.polymer.2014.09.066.

[23] Estevez R, Tijssens MGA, Van Der Giessen E. Modeling of the competition between shear yielding and crazing in glassy polymers. J Mech Phys Solids 2000;48:2585–617.

[24] Richter F, Schmidt HW. Supramolecular nucleating agents for poly(butylene terephthalate) based on 1,3,5-benzenetrisamides. Macromol Mater Eng 2013;298:190–200. https://doi.org/10.1002/mame.201200034.

[25] Zhao X, Yu J, Liang X, Huang Z, Li J, Peng S. Crystallization behaviors regulations and mechanical performances enhancement approaches of polylactic acid (PLA) biodegradable materials modified by organic nucleating agents. Int J Biol Macromol 2023;233. https://doi.org/10.1016/j.ijbiomac.2023.123581.

[26] Xin K, Wei Y, Xiong JX, Ni YP, Wang X, Xu YJ. Simultaneous strengthening and toughening of PLA with full recyclability enabled by resin-microsphere-modified L-lactide oligomers. Chem Eng J 2024;500. https://doi.org/10.1016/j.cej.2024.156743.

[27] Mohamad Ibrahim MN, Zakaria N, Sipaut CS, Sulaiman O, Hashim R. Chemical and thermal properties of lignins from oil palm biomass as a substitute for phenol in a phenol formaldehyde resin production. Carbohydr Polym 2011;86:112–9. https://doi.org/10.1016/j.carbpol.2011.04.018.

[28] Nogales A, Broza G, Roslaniec Z, Schulte K, Šics I, Hsiao BS, et al. Low percolation threshold in nanocomposites based on oxidized single wall carbon nanotubes and poly(butylene terephthalate). Macromolecules 2004;37:7669–72. https://doi.org/10.1021/ma049440r.

[29] Zhang W, Li J, Shang Y, Li H, Jiang S, An L. Temperature dependence of tensile behavior in poly(butylene terephthalate) with different crystallinity. Mater Des 2017;129:143–50. https://doi.org/10.1016/j.matdes.2017.04.035.

[30] Ravikumar K, Kiran K, Sreebalaji VS. Characterization of mechanical properties of aluminium/tungsten carbide composites. Measurement 2017;102:142–9. https://doi.org/10.1016/j.measurement.2017.01.045.

[31] Hoppe M, de Voogt P, Franz R. Oligomers in polyethylene naphthalate and polybutylene terephthalate – identification and exploring migration. Food Packag Shelf Life 2018;17:171–8. https://doi.org/10.1016/j.fpsl.2018.07.001.

[32] Chan JX, Wong JF, Hassan A, Othman N, Razak JA, Nirmal U, et al. Synthetic wollastonite nanofiber for polybutylene terephthalate nanocomposite: mechanical, thermal, tribological and flammability properties. Polymer (Guildf) 2022;256. https://doi.org/10.1016/j.polymer.2022.125259.

[33] Dai Y, Li K, Xiang Q, Ou M, Yang F, Liu J. Microstructure and tribology behaviors of WC coating fabricated by surface mechanical composite strengthening. Appl Surf Sci 2023;619. https://doi.org/10.1016/j.apsusc.2023.156759.

[34] Kim M, Lee J, Cho M, Kim J. Improvement of thermal and abrasion resistance performance of polyphenylene sulfide composite through 3-mercaptopropyl trimethoxysilane treatment of carbon fiber and graphene oxide fillers. Polym Test 2022;108. https://doi.org/10.1016/j.polymertesting.2022.107517.

[35] Soudmand BH, Shelesh-Nezhad K. Experimental investigation on the durability and failure modes of polybutylene terephthalate/calcium carbonate nanocomposite gears. Eng Fail Anal 2021;120. https://doi.org/10.1016/j.engfailanal.2020.105113.